Research Paper

Oxygen vacancies induced visible-light photocatalytic activities of $CaCu_3Ti_4O_{12}$ with controllable morphologies for antibiotic degradation

CrossMark

Reshalaiti Hailili[a,b], Zhi-Qiang Wang[c], Yingxuan Li[a], Yuanhao Wang[a], Virender K. Sharma[d,*], Xue-Qing Gong[c,*], Chuanyi Wang[a,*]

[a] Laboratory of Environmental Sciences and Technology, Xinjiang Technical Institute of Physics & Chemistry, Key Laboratory of Functional Materials and Devices for Special Environments, Chinese Academy of Sciences, Urumqi 830011, China
[b] The Graduate School of Chinese Academy of Science, Beijing 100049, China
[c] Key Laboratory for Advanced Materials, Centre for Computational Chemistry and Research Institute of Industrial Catalysis, School of Chemistry and Molecular Engineering, East China University of Science and Technology, Shanghai 200237, China
[d] Program for the Environment and Sustainability, Department of Environmental and Occupational Health, School of Public Health, Texas A & M University, College Station, TX 77843, USA

ARTICLE INFO

ABSTRACT

Searching photocatalysts with sufficient utilization of sunlight and elucidating relevant reaction mechanism are still grand challenges in the field of semiconductor photocatalysis. Herein, we developed a strategy towards morphology tailoring in conjunction with oxygen vacancy in the structure of double perovskite $CaCu_3Ti_4O_{12}$. Cube, polyhedron, nanorod and octahedron shaped $CaCu_3Ti_4O_{12}$ morphologies were obtained by varying the salt composition during molten salt synthesis, and their visible-light photocatalytic capacities were tested for degrading an antibiotic, tetracycline. The degradation process follows a first-order kinetics, and excellent photo-oxidation performance was observed for octahedron and nanorod shaped $CaCu_3Ti_4O_{12}$ giving degradation rate constants of $1.14 \times 10^{-1}\,min^{-1}$ and $8.40 \times 10^{-2}\,min^{-1}$, respectively, much higher than those of polyhedron and cube shapes (their rate constants were $5.10 \times 10^{-2}\,min^{-1}$ and $2.80 \times 10^{-2}\,min^{-1}$, respectively). The improved photoefficiency could be attributed to high abundant oxygen vacancies, surface properties, charge transfer and enhanced carrier separation due to the synergetic roles of active species, as is supported by active species trapping experiments and theoretical simulations. The detailed mechanism was proposed on the basis of crystal structure, unique morphology and spin trapping experiment, which reveals the roles of various active species for efficiency enhancement. The enhanced efficiency was further elucidated by theoretical investigations of density functional theory (DFT) calculations on the adsorption between tetracycline and $CaCu_3Ti_4O_{12}$. The findings reported here not only provide a green and rational design of high-performance photocatalysts but also show the applications ranged from catalysis to mitigation of polluted environment.

1. Introduction

A rapid development of industrialization in the past decades resulted in water pollution worldwide that has affected human health and ecology of the environment. Green and sustainable solution to global pollution is of utmost importance. Using solar light in conjunction with a catalyst is an attractive approach to treat polluted water [1–3]. Since early development of photoactive catalyst in 1960s, numerous studies have been performed in searching effective photocatalysts to treat a wide range of pollutants in water [4]. During photocatalytic treatment, remaining challenges are still insufficient sunlight utilization and ambiguous reaction mechanism. Early advancement in the field was focused on the ultraviolet (UV) light photocatalysts, which suffered from low yields of reactions and limited utilization of solar light (i.e., the UV accounts for only ~4% of solar irradiation) [5,6]. Therefore, in view of efficient utilization of solar light, the search of visible-light active photocatalysts became a main topic of intensive studies. Thus far, widely studied photocatalytic materials mainly include metal oxides (TiO_2, ZnO, WO_3) [7–10], sulfides (CdS) [11], oxynitrides [($Ga_{1-x}Zn_x$)($N_{1-x}O_x$)] [12], oxysulfide ($Sm_2Ti_2O_5S_2$) [13], heterojunctions [14–16], perovskite [17], and layered structured materials [18,19].

As photocatalysts, oxide semiconductors attract more attention because of their high stability, decent efficiency and relative low cost [20]. However, the large electronic band gap of the oxides becomes one

of main obstacles in efficiently utilizing solar light. It has been demonstrated that inserting transition metals into the structure of oxide semiconductors resulted in visible-light driven photocatalysts [21,22]. However, doping color metal into photocatalysts is not intrinsic and often reduces the catalytic efficiency because the dopant element may play as the recombination centers for the photoinduced electrons and holes. A promising way to address this challenging problem is to prepare complex oxide to tune the band gap and to achieve high efficiency under visible light irradiation without doping. Among various oxides, perovskite having diverse structures could overcome the drawbacks such as low efficiency, instability, and high electron−holes recombination rates [23,24]. Additionally, it is realized that modification with oxygen vacancies in their structures via different synthetic methods could also be an effective approach towards enhanced photoefficiency because these defects could trap the photoinduced chargers to accelerate electron−hole pairs separation [25,26]. Hence, design and synthesis of visible light active semiconductors with highly abundant oxygen defects to inhibit charge recombination and enhance its photocatalytic property is inspiring yet challenging task for the complex oxides.

$CaCu_3Ti_4O_{12}$ is a Ti-based perovskite, and mostly studied for dielectric property, though investigation of photocatalytic activity is still in its infancy [27,28]. Property of this newly exploited photocatalyst is related to synthetic methods and defect sites. The abundant oxygen vacancies and surface defects (e.g., Ti^{3+} and Cu^+) in the $CaCu_3Ti_4O_{12}$ not only make contributions to improve visible light absorption, but are deemed to be electron capture centers, which will reduce the carrier recombination, and thus leading to enhanced activity during photocatalytic process. Furthermore, in $CaCu_3Ti_4O_{12}$, the Cu 3d and O 2p levels can form a largely dispersed hybridized valence band, which also favors the separations of photogenerated electron−hole pairs and is beneficial to the oxidation reaction [27]. Therefore, in the view of unique structure property and visible light response, it is of great interest and obligatory to disclose the visible light driven photocatalytic activity of $CaCu_3Ti_4O_{12}$.

Choosing $CaCu_3Ti_4O_{12}$ as a promising photocatalyst and tetracycline as a probe molecule (as an emerging contaminant, releasing of tetracycline-like pharmaceutical residues poses threats to human health and ecobalance), the present work aims to: (i) synthesize of oxygen deficiency-containing $CaCu_3Ti_4O_{12}$ with controllable morphology using diverse salts in molten salt process, (ii) investigate morphology−property correlation and the enhanced visible light photocatalytical activity towards antibiotic decomposition and, (iii) clarify the origins of high performance effectiveness based on crystal structure, morphology, enhanced charge separation and theoretical investigations disclosing the adsorption and binding effects of tetracycline on $CaCu_3Ti_4O_{12}$. By far, the photocatalytic decomposition of pharmaceutical pollutants over distinct morphological $CaCu_3Ti_4O_{12}$ has not yet studied. The present study suggests that $CaCu_3Ti_4O_{12}$ *is* a promising visible-light active photocatalyst with high efficiency and good stability, and could offer new inspirations on other perovskite photocatalysts for environmental implementation.

2. Experimental section

2.1. Sample preparation

Flux treatment using various kinds of molten salts was performed to synthesize $CaCu_3Ti_4O_{12}$ in different salt systems. In a typical synthesis, metal oxides were used as raw materials, in which CaO (0.0049 mol), CuO (0.0146 mol), and TiO_2 (0.019 mol, 99.9%) were grinded in different salt systems (NaF, NaCl, NaBr, LiCl and KCl) with a given molar ratio for 60 min. Then, well-grounded mixtures were heated in the corundum crucible at 800 °C by increasing at a rate of 2 °C/min, and dwell them for 6 h. After the reaction, it was cooled slowly to room temperature at the rate of 1 °C/min, and the as-obtained samples were washed thoroughly with deionized water in order to remove the utilized molten salts, which were further examined by $AgNO_3$ solution. The final obtained products were dried at 80 °C in an oven for other general characterizations. The physical properties of the selected molten salts were listed in Table 1.

Table 1
Physical properties of the molten salts used, morphology and optical property of *Sample 1*–*Sample 5*.

Sample no.	Salt composition	Melting point (°C)	Boiling point (°C)	Morphology	Band gap (eV)
Sample 1	NaF	993	1695	Cube	1.6272
Sample 2	NaCl	801	1413	Polyhedron	2.0175
Sample 3	NaBr	747	1390	Cube	1.8970
Sample 4	LiCl	650	1350	Nanorods	2.4883
Sample 5	KCl	776	1420	Octahedron	2.0432

2.2. General remarks

The Scanning Electron Microscope (SEM) characterizations were performed on a Hitachi S-3500N scanning electron microscope. The Energy-disperse X-ray Analysis (EDXA) was performed on EDX G2T20136-5 energy-disperse X-ray instrument. Powder X−ray Diffraction (XRD) measurement of the studied samples was carried out using a Bruker AXS D8 Advance Diffractometer operating at 40 kV and 30 mA with a scan step width of 0.02° and a fixed counting time of 1 s/step using an graphite monochromator set for Cu Kα (λ = 1.5418 Å) radiation in the angular of 2 θ from 5° to 80°. Optical diffuse reflectance spectra of per 40.0 mg samples were recorded on a UV–vis spectrophotometer (Shimadzu SolidSpec−3700 DUV) in the wavelength range from 200 nm to 800 nm. The $BaSO_4$ was used as a reference for baseline correction. Electron Paramagnetic Resonance (EPR) spectra were measured at 4–298 K on a Bruker ElexsysE500 spectrometer working under the X-band and equipped with an Oxford cryostat with 20.0 mg of per samples. All the spectra were recorded at 100 K and the g values were determined by calibration with DPPH (Bruker spectrometer) standard. The Brunauer–Emmett–Teller (BET) surface areas were determined from the N_2 adsorption−desorption isotherms recorded at 77 K on a Quantachrome Instrument (QUADRASORB IQ) after the samples were degassed at 180 °C for 3 h. Infrared Spectra (IR) were recorded on Bruker Optics TENSOR 27 Fourier transform infrared spectrometer in the range from 400 cm^{-1} to 4000 cm^{-1}.

2.3. Photocatalytic activity evaluations

2.3.1. Photocatalytic activity test

The photocatalytic activity of the obtained samples was evaluated by the decomposition of a model pollutant, antibiotic tetracycline. For a typical experiment, 40.0 mg of a prepared $CaCu_3Ti_4O_{12}$ sample catalyst was dispersed in a tubular quartz reactor containing 100 mL of 1.0×10^{-5} mol L^{-1} tetracycline aqueous solution. The mixture was put in a beaker, and stirred for 30 min in the absence of light to attain adsorption equilibrium on the catalyst surface. The reactor was irradiated with a 300 W Xe lamp (PLS−SXE300, Perfect Light Company, Beijing, China), which was equipped with a cutoff filter (420 nm) to obtain visible light source. The photon flux of the incident light was determined using a Ray virtual irradiatometer (1916-C, light intensity is about 500 mW cm^{-2} with an error value < 5%). During photocatalytic reaction, samples were taken at specific times and centrifuged for 30 min to discard any sediment. Then the degradation product at a given internal time was monitored through optical absorption, i.e., the concentration changes of tetracycline was preliminarily determined by UV–vis spectrophotometer (UV-1800, Shimadzu, Japan). For the accurate analysis, high performance liquid chromatography (HPLC, UltiMate3000, USA) measurements were carried out. The 1.0 mL of

suspension samples were taken at certain reaction time intervals, which were filtration with 0.45 μm filter before analysis by a HPLC, which is equipped with a VWD detector (wavelength was at 355.0 nm) and a Cosmosil 5C18-MS-II (particle size 5.0 μm, 4.6 × 250 mm). The 40% methanol and 60% water (with 1% phosphoric acid, pH = 3.0) were used as mobile-phase at a flow rate of 1.0 mol L^{-1} at 35 °C. The TOC measurements of centrifuged samples were measured on a vario TOC (Elementar, Germany) analyzer.

2.3.2. Catalyst stability test

For the examination of the stability of the catalyst for tetracycline degradation, the recycle test was investigated by six runs of photocomposition at the same reaction conditions. In a typical procedure, the 40.0 mg of catalyst was dispersed in 100 mL of 1.0×10^{-5} mol L^{-1} tetracycline solution for the first cycle. The sample was collected and combined together, and then was subsequently immersed into fresh tetracycline aqueous solution (1.0×10^{-5} mol L^{-1}) for another cycle of examination. The above procedure was performed for six times. To the further confirmation of sample stability, the catalyst was filtered after the reaction dried at 80 °C for XRD and FTIR measurement.

2.3.3. Detection of active species

Active species contributing to the photodegradation activity were identified by scavenger tests and Electron Spin Resonance (ESR) measurements. In the present work, isopropyl alcohol (IPA), ammonium oxalate (AO), p−benzoquinone (PBQ) and silver nitrate ($AgNO_3$) were used as hydroxide ($\cdot OH$), hole (h^+), superoxide ($\cdot O_2^-$) and electron (e^-) scavenger, respectively. A chosen scavenger was added to the catalyst−tetracycline suspension and stirred for 30 min in the dark before the photodegradation experiment at the same reaction conditions. To verify the formation of reactive radicals responsible for tetracycline oxidation reaction, the 5, 5−dimethyl-l-pyrroline-*N*-oxide (DMPO) was used as the spin trapper to capture $\cdot O_2^-$ and $\cdot OH$, the 2, 2, 6, 6−tetramethylpiperidine-1-oxyl (TEMPO) was used to detect electrons, and the 1−hydroxy-3-carboxy-2, 2, 5, 5-tetramethylpyrrolidine (CPH) used as the spin trapper to detect photoinduced holes. In a typical procedure, per 5.0 mg of sample was dispersed in 2.5 mL of methanol/water (HPLC grade CH_3OH for $\cdot O_2^-$ and the water as $\cdot OH$ trapper), and it was stirred for about 30 s to obtained uniform dispersed suspension, in which the 30.0 μL DMPO/TEMPO was added followed by above procedure. Then, the mixture was irradiated with 300 W Xe lamp for 0−5 min, and then was analyzed by EPR using a Bruker Elexys E500 spectrometer.

2.4. Density functional theory computational methodology

Density functional theory (DFT) calculations on $CaCu_3Ti_4O_{12}$ were performed using the Vienna *ab initio* Simulation Package (VASP) [29]. All structures and adsorption energies were optimized with slab models. To improve the calculation efficiency, core electrons were replaced by the projector augmented wave pseudo-potentials and the generalized gradient approximation of Perdew, Burke, and Ernzernhof was used for exchange and correlation [30]. The plane wave basis sets with a maximum kinetic energy of 400 eV were used. The vacuum between slabs was set to ~15.0 Å to eliminate the interaction between neighboring slabs. A 2 × 2 surface cell was used to construct a three-layer $CaCu_3Ti_4O_{12}$ (101) slab, and the top half of the $CaCu_3Ti_4O_{12}$ (101) slab were relaxed.

3. Results and discussion

3.1. Synthesis and characterization of photocatalysts

Fig. 1 exhibits typical morphologies of the samples obtained by molten salt synthesis (MSS), in which the morphologies of the prepared samples vary in different salt systems. During the synthesis, employed

molten salts were ionized to cations and anions, which played crucial roles in reducing energy on particular surface and shaping the morphology of the $CaCu_3Ti_4O_{12}$ crystals. In case of NaF used as a molten salt, the corresponding *Sample 1* exhibits cubic shaped morphology with (001) exposed facet (Fig. 1a). The ionization of molten salt NaF gave Na^+ and F^-, these generated F^- ions play crucial roles to generating facet morphology of crystals. Forming (001) facet with the assistance of F^- in the system such as HF, NH_4F, $NaBF_4$, NaF, TiF_4 and $(NH_4)_2TiF_6$ has been reported previously [31–36]. As seen in Fig. 1b, when the employed salt changed to NaCl, *Sample 2* shows typical polyhedron with high yields ~95%, and uniformity. *Sample 3* (obtained in NaBr) is edge truncated cubes with three exposed facets (001), (010) and (100) because of low surface energies for these facets (Fig. 1c). When the salt composition changed to LiCl, the observed morphology is long nanorods with trace amount of cubes as exhibiting in *Sample 4* (yield of 94% based on nanorods). It is likely that the solubility of $CaCu_3Ti_4O_{12}$ in LiCl and smaller ionic radius of Li^+ (92 pm) may lead to high growth rates of some facets towards specific orientation to yield long nanorods in *Sample 4* (Fig. 1d). As depicted in the inset of Fig. 1e, with (101) and (111) exposed facets, octahedron morphology was observed in *Sample 5* with the assistance of KCl salt in the system. It has been demonstrated that during the crystal growth process, crystal facet with high surface energy gradually declined or easily disappeared [31]. Generally, in the specific growth environment, e.g., solvents or fluxes like molten salts have fast mobility and strong electrostatic interactions occur between ions and surfaces; the higher the surface energy, the faster the growth rate. Thus, the surface with low energy exposed easily and orientated crystal faces were obtained in the present study. Herein, as-obtained samples give high yield and phase purity, for instance in *Sample 5*, highly uniformed octahedron with 92% of yields were observed and its corresponding element compositions were testified by energy−dispersive spectroscopy (EDS) analysis, further confirming the *Sample 5* were consist of only Ca, Cu, Ti and O (Fig. 1f).

The first step of molten salt synthesis was gradual ionization of utilized salts as increasing reaction temperature to reach its melting points and generate cations and ions [37,38]. These ionized cations (Li^+, Na^+, K^+) and anions (F^-, Cl^-, Br^-) would adsorbed on the surface of $CaCu_3Ti_4O_{12}$, directly influencing the growth rates, directions and reducing energy on particular surface to shape the nanorods, polyhedron and octahedron morphology of the $CaCu_3Ti_4O_{12}$ crystal. When various anions were applied in synthesis with the same cation (Na^+) as for *Sample 1*, *Sample 2* and *Sample 3*, polyhedrons were obtained, and the same anionic system (Cl^-) gave diverse morphologies such as nanorods and polyhedrons (Fig. 1a–c). The interaction between ions follows the order $Li^+ > Na^+ > K^+$, among which Li^+ acquires the strongest contacts because of the higher electrons on the Li^+, and this in turn results in the relatively weaker binding effects. Therefore, the growth behavior of *Sample 4* into significant nanorods might have been driven by these effects. However, the capping effects of K^+ could result in octahedron morphology with index facets of *Sample 5* in KCl salt system. The ionic radius of K^+ (139 pm) [39] is very close to Ca^{2+} (134 pm), and thereby accelerate the interactions and substitutions of these ions. Very small amount of the K^+ ions are adsorbed on the surface to interact with Ca^{2+} due to the effects of electrostatic force, which can affect the surface adsorption to form octahedron shaped morphology. Thus, the ionic radius directly affected the morphology of as-obtained samples and the introduced salt ions were not incorporated into the bulk. Herein, besides cation radius, the ionic interactions, viscosities of salts, and solubility of $CaCu_3Ti_4O_{12}$ samples in salt systems altogether lead to the formation of assorted crystal shapes of $CaCu_3Ti_4O_{12}$ with some etches and cracks, indicating there was a self-etching process and defect sites occurring during the crystal growth. Overall, it can be confirmed that variation in salt compositions could result in diverse morphologies and gave various exposed polyhedral facets at the same preparation conditions, thus salt-depending crystal growth performance existed in $CaCu_3Ti_4O_{12}$ samples.

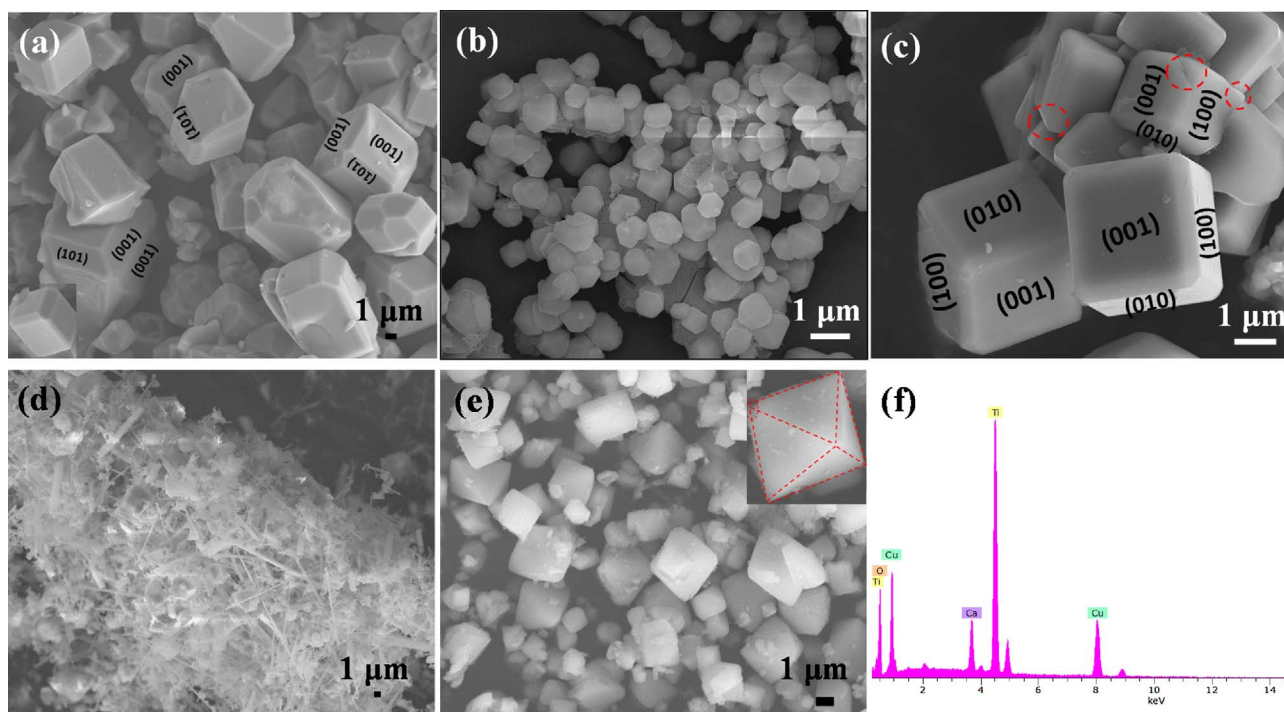**Fig. 1.** (a) Cube shaped $CaCu_3Ti_4O_{12}$ (*Sample 1*) obtained in molten salt NaF; (b) High yield and uniform polyhedron morphology of $CaCu_3Ti_4O_{12}$ (*Sample 2*) obtained in molten salt NaCl; (c) Cube shaped $CaCu_3Ti_4O_{12}$ (*Sample 3*) prepared in molten salt NaBr; (d) Nanorods of $CaCu_3Ti_4O_{12}$ (*Sample 4*) obtained in molten salt LiCl; (e) Octahedron shaped $CaCu_3Ti_4O_{12}$ (*Sample 5*) fabricated in molten salt KCl. The inset is the magnified image showing detailed octahedron morphology; (f) EDS spectrum of *Sample 5*.

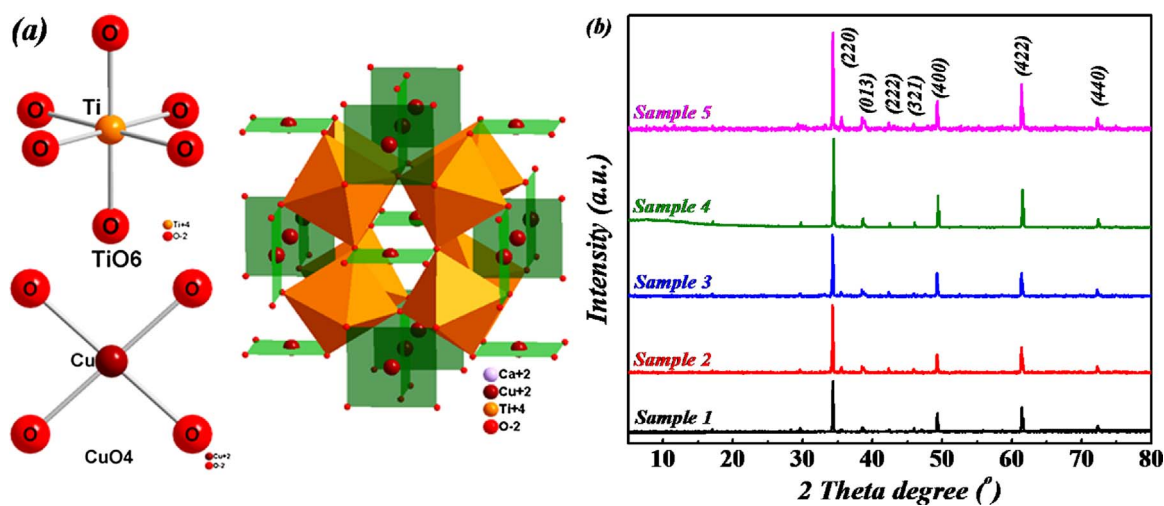**Fig. 2.** (a) Crystal structure of $CaCu_3Ti_4O_{12}$ with square planner CuO_4 and TiO_6 octahedra; (b) XRD patterns of *Sample 1–Sample 5*.
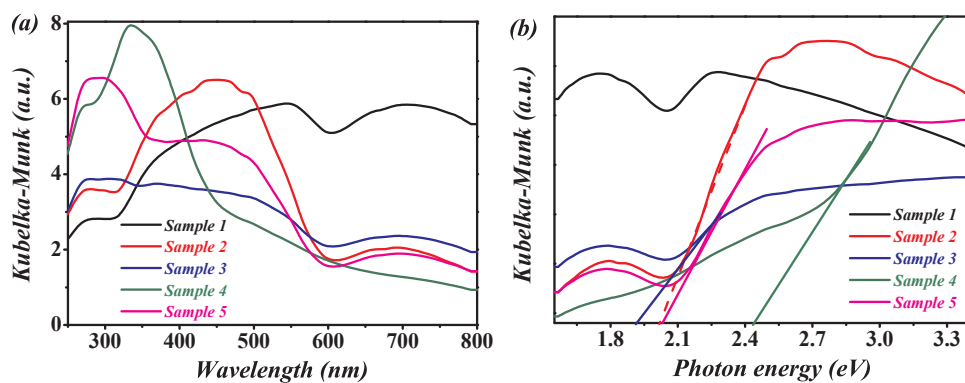

Fig. 3. (a) Room − temperature UV–vis DRS absorptions; (b) The corresponding plot of absorption coefficient plotted versus photon energy $h\nu$ of *Sample 1–Sample 5*.

$CaCu_3Ti_4O_{12}$ is a Ti-based double perovskite classified as cubic structure containing open–shell CuO_4 and TiO_6 units (Fig. 2a). As revealed by XRD results in Fig. 2b, the resulted diffraction patterns of *Sample 1–Sample 5* match very well and all the diffraction peaks of samples can be attributed to the standard $CaCu_3Ti_4O_{12}$ phase (Cubic crystal system, $Im3$ (204) space group, lattice constant a = 7.391 Å, JCPDS card No. $75-2188$). The comparatively sharp and narrow diffraction peaks indicate high crystallinity and phase purity of as-obtained samples. No characteristic peaks are observed for other impurities such as CuO and CaO. Besides, the intensity of the (220) peak in the patterns of the studied samples is relatively stronger, indicating there are more exposed faces.

The optical properties of the samples were investigated by the UV–visible diffuse reflectance spectra. All samples display strong optical absorptions, which are attributed to the hybridized valence band (VB) from Cu 3d–O 2p to conduction band (CB) with Ti–3d states (Fig. 3a). The band gaps of prepared samples were determined when the spectra were converted to Kubelka–Munk function (Fig. 3b) [40]. Samples show significant visible-light responses within band gap range 1.627 eV–2.488 eV, corresponding to the charge transition from ground state to excited state between $Cu^{2+} + Ti^{4+} \rightarrow Cu^{3+} + Ti^{3+}$. All the measured band edges are quiet reasonable and consistent with reported band gap $E_g \geq 1.500$ eV [26]. One can be found from DRS results that the light absorption gives around 300 nm–600 nm and 700 nm, representing different excitations in $CaCu_3Ti_4O_{12}$. The electron transportation from $O\ 2p^6$ to $Ti\ 3d^0$ excitation comes from TiO_6 octahedrons results in the absorption at 366 nm. The observed strong peaks around the absorption of 300 nm–600 nm in *Sample 2–Sample 5* mainly comes from excitation of the $Cu\ 3d^9$ transition $d_{x^2-y^2} \rightarrow d_{xy}$, indicating the hybridization of the O 2p and Cu 3d orbital and higher covalent character for the Cu–O bond than for the Ti–O bond [26]. Besides, the light absorptions are significantly decreased and tailed beyond 700 nm, indicating existence of defect sites in the structure. The variable light absorptions of samples are caused by the increasing oxygen vacancy concentration on $CaCu_3Ti_4O_{12}$, which is further testified by electron paramagnetic resonance (EPR) analysis.

Room-temperature EPR measurements were carried out to further explore the relative concentration and distribution of defects on samples (Fig. 4a). The broadening of the EPR line-width of $CaCu_3Ti_4O_{12}$ was attributed to the copper oxygen (Cu–O) vacancy, appeared at around g = 2.0–2.5 [41], as observed in samples with different intensities and widths. As shown in Fig. 4b, larger line widths with stronger intensities were observed in samples (*Sample 2, Sample 4* and *Sample 5*) at around g = 2.04–2.09, indicating high oxygen vacancy concentration while the relatively weaker and lower signals were found in *Sample 1* and *Sample 3* at about g = 2.07–2.09. The strong and broad EPR signals of *Sample 2*, *Sample 4*, and *Sample 5* are almost in the same position as that of *Sample 1* and *Sample 3* since all samples have same content of Cu. Wide and high intensity of EPR signals in *Sample 4* and *Sample 5* suggests the existence of higher abundant oxygen vacancies and more other defect sites (V_o, Cu^+ and Ti^{3+}) than other samples.

Therefore, better photocatalytic efficiency would be expected for *Sample 4* and *Sample 5*.

As a typical principle of MSS, the prior option and basic demand are the selected salts should be with low melting point and easy washable properties in order to accelerate reaction and achieve reduced synthesis temperature. Herein, to examine halogen (F, Cl, Br) and alkali (Li, Na, K) effects on the morphology of $CaCu_3Ti_4O_{12}$, we select following salts instead of combined salt system such as $NaCl-Na_2SO_4$. The properties of utilized molten salts, morphologies and optical properties of samples are summarized in Table 1.

3.2. Evaluation of photocatalytic activity

The visible light photocatalytic efficiency of $CaCu_3Ti_4O_{12}$ samples was tested using a target compound, tetracycline (see molecular structure in Fig. S1, in the Supporting Information). Tetracycline (TC), a well-known broad spectrum antibiotic that, released to the environment and poses threat to human health and ecology [42]. The maximum absorption at 355 nm of TC gradually decreases with increases of visible light irradiation time and complete degradation of TC was observed within 50 min, which was further confirmed by HPLC analysis. As shown in Fig. 5a, after 30 min irradiation of visible light, the remaining concentration of TC using *Sample 5* is nearly zero. After 50 min irradiation of visible light, the TC removal percentages over different morphological $CaCu_3Ti_4O_{12}$ samples are as follows: *Sample 5* (99.1%) > *Sample 4* (97.1%) > *Sample 2* (87.3%) > *Sample 3* (66.8%) > *Sample 1* (7.91%). The *Sample 5* shows relatively highest degradation performance compared to other samples. As generally accepted, photoactivity of perovskite ABO_3 is mainly determined by B sites [1]. For $CaCu_3Ti_4O_{12}$, B sites are comprised of TiO_6, and its excitation directly influences the photocatalytic activity of samples. As illustrated in DRS analysis, the light absorption at 366 nm is mainly comes from TiO_6 octahedrons, which is not strong in *Sample 1*. Additionally, compared with *Sample 2–Sample 5*, the *Sample 1* has the narrowest band gap, lowest oxygen vacancies, naught hybridization of Cu 3d $-$ O 2p, giving trace amount of excitation of electron to CB (Ti 3d) and displaying the poorest photoefficiency. *Sample 2* shows higher removal efficiency of TC (i., 87.3%) though it has the lowest surface area (0.0940 $m^2\ g^{-1}$, Fig. 5b) but higher oxygen vacancy than that of *Sample 1*. With (001), (100) and (010) exposed facets, the *Sample 3* acquires trace amounts of oxygen vacancies. This resulted in enhanced crystallinity and decreased defects in *Sample 3*, which causes low removal efficiency of TC. Significantly, with the nanorods morphology, *Sample 4* shows high performance in TC decomposition due to orientated crystal growth, which leads to fast charge transfer and highly abundant defects. In the KCl molten salt, *Sample 5* has octahedron shaped crystals with (101) exposed facets and high abundant defects (metal and oxygen defects), hence displays the highest photocatalytic activity. Overall, the *Sample 2*, *Sample 4* and *Sample 5* display relatively higher efficiency among as-obtained samples, which is closely related to oxygen vacancy.

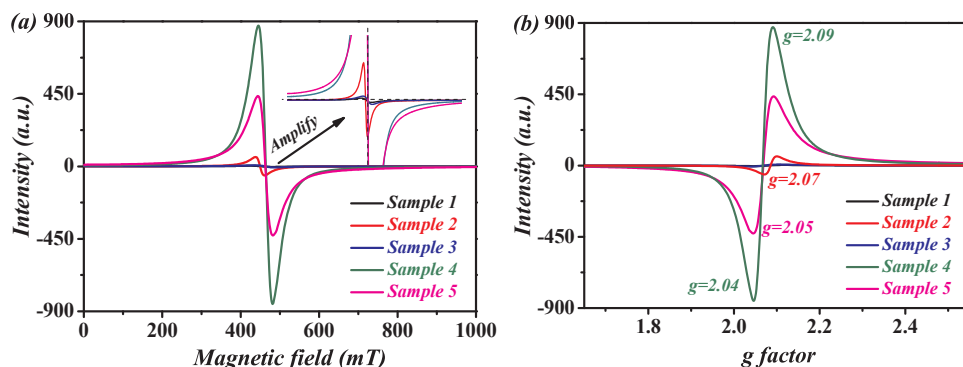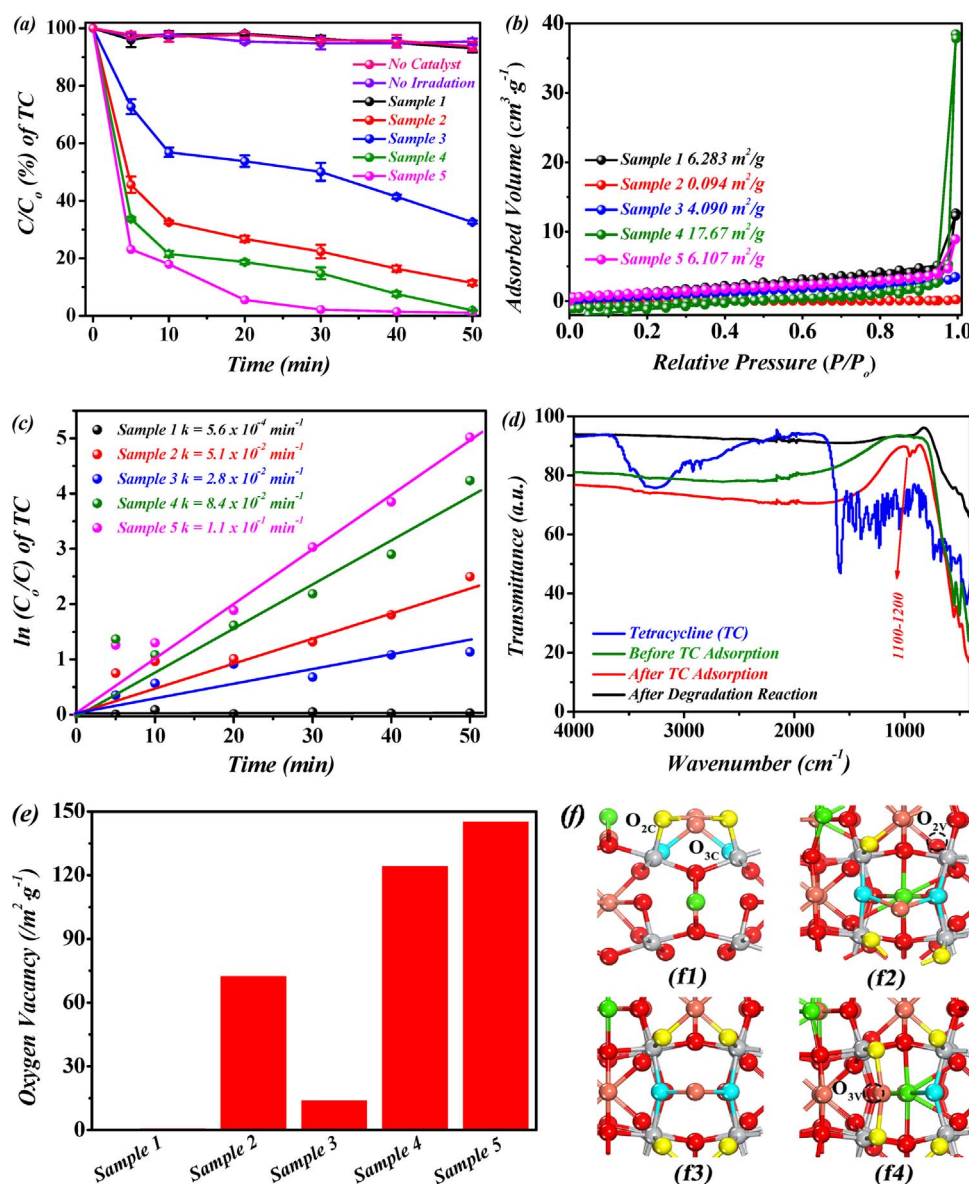To quantitatively compare the photocatalytic performances of

Fig. 5. (a) Degradation of TC in visible light irradiation using different samples of $CaCu_3Ti_4O_{12}$; (b) Nitrogen adsorption–desorption isotherms of as-obtained *Sample 1−Sample 5*; (c) Plot of $\ln(C_o/C)$ versus irradiation time; (d) FTIR spectra of TC, the *Sample 5* before and after TC adsorption, and after irradiation for 60 min with visible light; (e) Normalized oxygen vacancy percentages on *Sample 1–Sample 5*; (f) Oxygen vacancy on the surface of *Sample 5;* f1, $CaCu_3Ti_4O_{12}−001$ (side view); f2, $CaCu_3Ti_4O_{12}−001$ (top view); f3, $CaCu_3Ti_4O_{12}−001−2\,v$ (top view); f4, $CaCu_3Ti_4O_{12}−001−3\,v$ (top view); the structures are color-coded as follows: green, Ca; light grey, Ti; brick red, Cu; red, O; yellow, two coordinated O; blue, three coordinated O. (For interpretation of the references to colour in this figure legend, the reader is referred to the web version of this article.)

different morphological samples, the kinetics of the TC photodegradation over as-obtained samples are evaluated by using pseudo first-order kinetics equation [43]:

$$\ln (C_o/C) = kt$$

where C_o is the initial TC concentration, C is the varied TC concentration at an irradiation time t, and k is the pseudo-first-order rate constant. As depicted in Fig. 5c, the samples show linear relationship between $\ln(C_o/C)$ and irradiation time (t), indicating that the photocatalytic degradation of TC follows the first-order kinetics. The apparent rate constants k of the TC photodegradation in the presence of *Sample 1–Sample 5* are 5.6×10^{-4} min^{-1}, 5.1×10^{-2} min^{-1}, 2.8×10^{-2} min^{-1}, 8.4×10^{-2} and 1.1×10^{-1} min^{-1}, respectively with the standard errors of $S_E < 0.1$. This is in good agreement with the diverse morphologies of $CaCu_3Ti_4O_{12}$ samples, giving variation in photocatalytic activity of degrading TC.

It is well-accepted that the higher surface area provides more active sites, which could accelerate effective adsorption and thus enhance photocatalytic activity. The TC adsorption test was carried out and the effective adsorption was understood by conducting FTIR measurements of the TC before and after adsorption of *Sample 5* (Fig. 5d). After the TC adsorption on the surfaces of *Sample 5*, the newly formed vibrations

were observed at around 1000 cm^{-1}–1200 cm^{-1}, attributed to the C–N amine stretching vibration of TC molecule. This suggests that TC was efficiently adsorbed onto the surface of *Sample 5*. After the photocatalytic reaction, the C–N amine stretching vibration of TC molecule disappears, indicating the complete degradation of TC. More interestingly, the *Sample 1* has second higher surface area (6.28 m^2 g^{-1}), though it shows the lowest efficiency of TC photodegradation. Both *Sample 1* and *Sample 5* acquire similar specific surface areas (6.28 m^2 g^{-1} and 6.10 m^2 g^{-1}, respectively), and the measured surface area normalized pseudo-first order rate constant for *Sample 5* (1.8×10^{-2} g min^{-1} m^{-2}) is $\sim 2.02 \times 10^2$ fold higher than for *Sample 1* (8.91×10^{-5} g min^{-1} m^{-2}). To correlate the oxygen vacancy with efficiency, the BET surface area is taken into account, and it is found that the photocatalytic efficiency and oxygen vacancy give same order in *Sample 1–Sample 5* when the defects are normalized to sample's surface areas (Fig. 5e).

The further theoretical investigations were conducted to confirm active defects on sample surface, on which the various coordination states of oxygen atoms were analyzed. The results demonstrated that the formation energies of two and three coordinated oxygen vacancies (O_{2V} and O_{3V}) are 0.895 eV and 1.845 eV, respectively (Fig. 5f1–f4). This suggests that oxygen vacancies can be formed in samples (i.,
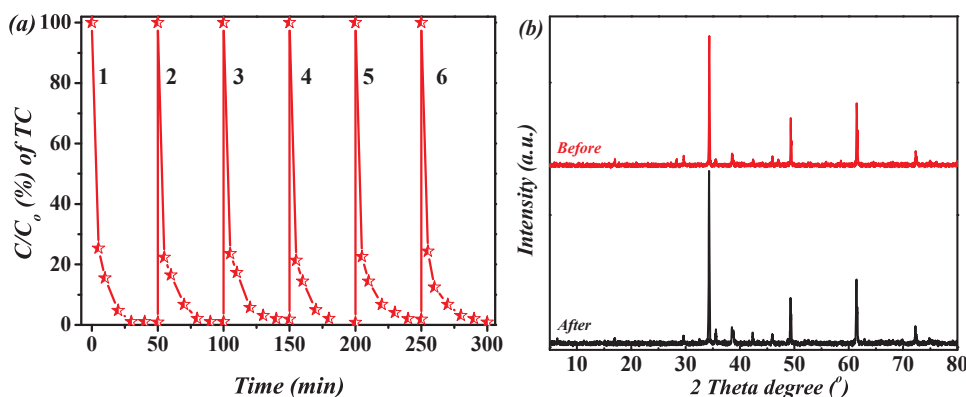
Sample 5) and these defect sites would provide more active sites and cause effective separation of electron–hole pairs to yield high efficiency, thus the oxygen vacancy is determine the photocatalytic activity of samples rather than the surface area.

Prior to the practical application of a photocatalyst, two factors should be taken into account, photoefficiency and stability. The comparative TC degradation of six successive catalytic cycles is shown in Fig. 6a. In each cyclic degradation test, nearly 98% of TC decomposition was achieved after 50 min of visible light irradiation, indicating the stability of samples (the recyclable decompositions of TC over other $CaCu_3Ti_4O_{12}$ samples are given in Fig. S2, in the Supporting Information). After the photocatalytic reaction, the sample could be easily filtered and collected without suffering from cumbersome procedures of separating the suspension of catalysts from the multi-phase reaction system. The structural stability also is verified by comparative XRD and FTIR analysis before and after the reaction (Figs. 6 b and S3, in the Supporting Information). Results clearly show that the surfaces of *Sample 5* were unchanged even after six runs of photocatalytic reactions (300 min). Furthermore, no apparent exhaustion and photocorrosion took place during photocatalytic process.

3.3. Clarification of the degradation mechanism and theoretical investigations

The optical property, energy band configuration, and effective charge production are imperative to photocatalytic activity, which determine the absorption of incident photons, the photoexcitation of electron−hole pairs, the migration and the redox capabilities of carriers [44,45]. Under visible light illumination, the appropriate band configurations of $CaCu_3Ti_4O_{12}$ renders samples visible light responsible. The CB and VB positions of $CaCu_3Ti_4O_{12}$ with respect to potential of active species are calculated empirically according to relationship between band edge energy and electronegativity, which can be expressed as following [46,47]:

$$E_{CB} = \chi - E_c - \frac{1}{2}E_g \quad E_{VB} = E_{CB} + E_g$$

where E_{CB} is the conduction band potential, χ is absolute electronegativity of semiconductor, calculated as the geometric mean of absolute electronegativity of consisting elements $\chi = (\chi_A^a * \chi_B^b * \chi_C^c)^{1/(a+b+c)}$ of semiconductor $A_aB_bC_c$; E_C is a scale factor usually taken as -4.5 eV with respect to the normal hydrogen electrode (NHE scale), and E_g is the band gap of semiconductor.

Herein, for $CaCu_3Ti_4O_{12}$, the value of χ is about $\{(\chi_{Ca}\chi_{Cu}^3\chi_{Ti}^4\chi_O^{12})^{1/20}\}$, and the electronegativity of Ca, Cu, Ti and O is 2.20, 4.48, 3.45 and 7.54, respectively. Thus, the corresponding band edges position of CB is determined to be -0.136 eV and the position of its VB is estimated to be 2.35 eV (*Sample 4*). The VB of $CaCu_3Ti_4O_{12}$ is between the OH$^-$/·OH and the H$_2$O/·OH potentials, indicating the tendency to produce OH$^-$/·OH (Fig. 7). Hence, the ·OH radicals can be
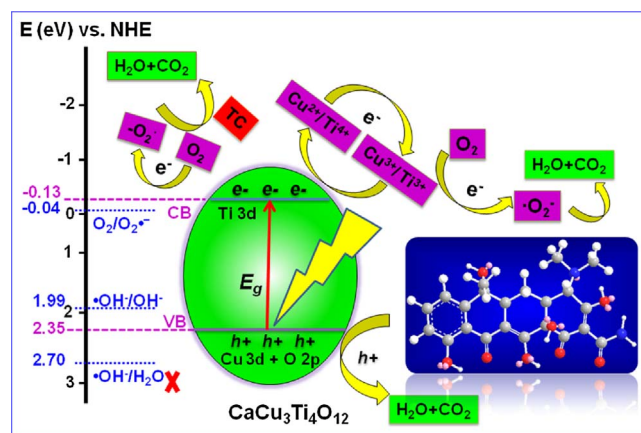

Fig. 7. Photodegradation mechanism of TC over $CaCu_3Ti_4O_{12}$ under visible light irradiation.

generated with the strong oxidation role of photoinduced holes on the VB (Cu 3d–O 2p) to attack TC or directly oxidize surface adsorbed TC. The potentials of CB (Ti 3d) is more negative than the potential of O_2/·O_2^- that is suitable for ·O_2^- formation. This is supported by radical trapping experiments, which are described in section of the detection of reactive species in detail. The dissolved O_2 in solution and the O_2 on the surface of $CaCu_3Ti_4O_{12}$ can capture the photogenerated electrons to yield ·O_2^-. In this way, the photogenerated electrons would not migrate and react at $CaCu_3Ti_4O_{12}$ surface, which could accelerate the carrier separation. With the synergetic effects of photogenerated electrons and holes, TC molecules lose the methyls from the tertiary amine and make removal of a hydroxyl to break down the structure, thus benefitting the efficient separation of electron–hole pairs.

Oxygen vacancy and electron transferring in metals are relevant. From the view point of crystal structure, the open–shell Cu^{2+} and TiO_6 octahedral coexist in $CaCu_3Ti_4O_{12}$, and the electron transportation occurs between metals ($Ti^{4+} + Cu^{2+} \rightarrow Ti^{3+} + Cu^{3+}$). The photogenerated electrons transfer to the Ti^{4+} in the TiO_6 to form Ti^{3+}. Moreover, the surface adsorbed oxygen molecules in $CaCu_3Ti_4O_{12}$–TC suspension form superoxide radicals (·O_2^-) via electron transfer from Ti^{3+} to O_2 because of the strong reducing ability of Ti^{3+}, which is further oxidized to Ti^{4+} ions. Therefore, the electron transfer between Ti^{3+}–Ti^{4+} also contribute for efficient separation of carriers. Such active radicals could increase the electron donor density to promote charge transport, leading to high photooxidation activity towards TC degradation. On the other hand, the presences of V_o indicate the formation of Cu^+, and enhance the charge separation. Thus, the enhancements in TC decomposition in samples are mainly related to the charge transformations and surface point defects, which could promote carrier separation.

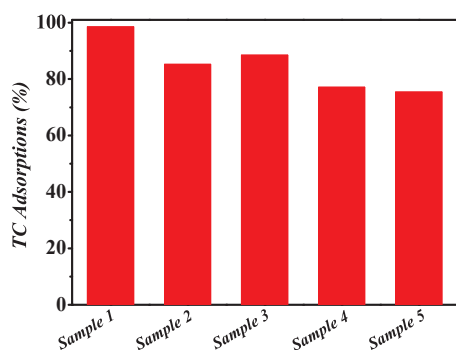The surface property is critical to photocatalytic activities. In the

Fig. 8. The adsorption curve of TC in the presence of the *Sample 1–Sample 5*.

process of photooxidation experiment, the first step should be adsorption of reactants ($\cdot O_2^-$, pollutants, i.e., TC) on to the surface of photocatalysts. For surface adsorption, it is not clear how the adsorption interactions between TC and photocatalyst, and the consequent photoactivity. To clarify this, an adsorption experiment was carried out. The *Sample 5* acquires relatively high TC adsorption (24.57%) compared with other samples, about 16.6 times higher than that of adsorption in the presence of *Sample 1*. More interestingly, the *Sample 4* posses the largest surface area (17.67 $m^2\,g^{-1}$), though the highest adsorption was obtained in *Sample 5*, indicating that the interaction of TC with $CaCu_3Ti_4O_{12}$ is stronger in the aqueous solution (Fig. 8).

In order to further understand the interactions between $CaCu_3Ti_4O_{12}$ and TC, the adsorption was calculated. Fig. 9 illustrates the calculated adsorption structure of the TC molecule on the surface of $CaCu_3Ti_4O_{12}$. It can be seen from Fig. 9a that the adsorption structure involves the O_1–Cu, O_2–Ti_1, O_3–Ti_1 and O_4–Ti_2 bonds, and the corresponding bond length of O_1–Cu, O_2–Ti_1, O_3–Ti_1 and O_4–Ti_2 are 2.489 Å, 2.078 Å, 2.365 Å and 1.950 Å, respectively. Fig. 9b shows that O 2p orbital and M 3d (M for Cu and Ti) orbital have a great overlapping in the area (bonding states) left to the fermi level, suggesting that the O and M form strong covalent bonds, especially for the O–Ti bond. In other words, the TC adsorption strength at $CaCu_3Ti_4O_{12}$ could be increased, which agrees well with the experimental result (Fig. 8).

The chemical environment of the solution may be of the primary factor. As shown in Fig. 10a, the TC shows protonation–deprotonation behavior, and in the presence of dimethylammonium (C4) group, phenolic diketone moiety (C10−C12), and the tricarbonyl system (C1–C3), the TC exhibits amphoteric character with pK_a at about 3.32, 7.78 and 9.58, respectively [48]. When the pH value of solution is < 3.32, TC is positively charged; at pH 3.32–7.78, mainly with neutral form as TC and or anionic, and under this pH condition, the TC would be in its zwitterionic TC form; when the pH is ≥7.78–9.58, TC is mostly with negative charges. At higher acid environments, the

hydrolization takes place, which are favorable to attacking and removing $-N(CH_3)_2$ groups due to the formation of NH_4^+–N by easy breaking of C–N under the light irradiation, beneficial for efficient adsorption of TC, thus resulting in high performance. Variations in pH have also impact on physiochemical properties such as surface charge and adsorption interactions of TC molecules on the photocatalyst. The photodegradation at different pHs was thus examined. Initially, the pH dependent UV–vis spectra of TC were collected and showed that TC displayed similar absorption features in the pH range from 1.0 to 7.0. However, in the pH range from 9.0 to 13.0, the peak position shifts to longer wavelength, and the peak intensity becomes stronger. As the pH increases in the range 1.0–13.0, more favorable photolysis of TC is observed, indicating electronic structure changes in TC. Additionally, TC shows higher visible light absorption in the alkaline solution than in the acidic environment (Fig. S4, in the Supporting Information), implying that the photoexcitation of TC in acid solution is lower than that in neutral or high alkaline environment. Fig. 10b exhibits the degradation of TC without $CaCu_3Ti_4O_{12}$ photocatalyst under visible irradiation at pH of 3.0, 7.0, 9.0 and 13.0, respectively. Fig. 10c shows the degradation of TC in the presence of $CaCu_3Ti_4O_{12}$ photocatalyst under visible light irradiation over wide range of pH values from 1.0 to 13.0. Clearly, TC displays relatively higher degradation in alkaline media, evincing that TC is inclining to give higher photolysis at alkaline solution over the studied *Sample 5*. After 50 min visible light irradiation, the degradation efficiency is greatly enhanced from 1.321% (pH = 1.0) to 98.95% (pH = 13.0) by the increasing of pH in the range of 1.0–13.0 (Fig. 10d). Thereby, the influence of pH in $CaCu_3Ti_4O_{12}$–TC systems is vital.

Besides the oxygen vacancies and chemical environments of reaction solution, the roles of involved active radicals are relevant. When the *Sample* is irradiated by visible light, electron–hole pairs are formed. The photogenerated holes (h^+) have strong oxidation ability, thus react with surface adsorbed H_2O to produce reactive hydroxyl radicals ($\cdot OH$) or directly oxidize surface adsorbed organic molecules. The electrons (e^-) can induce reduction reaction, as scavenged by O_2 to yield superoxide radicals ($\cdot O_2^-$), which can also degrade organics. Therefore, the commonly related active species e.g., $\cdot OH$, $\cdot O_2^-$ anions, h^+ and e^- are expected to be involved in the photocatalytic degradation of TC [1−3]. A trapping methodology was applied to determine which of the active radicals are contributing to degradation of TC by the $CaCu_3Ti_4O_{12}$ photocatalyst. Isopropanol (IPA) was used as $\cdot OH$ scavenger, $p-$benzoquinone (PBQ) for quenching $\cdot O_2^-$, ammonium oxalate (AO) was applied as h^+ scavenger, and silver nitrate ($AgNO_3$) employed as an e^- trapping agent, respectively. When IPA was introduced in the system, the degradation was slightly affected, but still showed decomposition of TC (Fig. 11a). This suggests that the $\cdot OH$ has limited role or almost makes no contribution in degrading TC. Moreover, 59.3% of TC degradation was obtained when $AgNO_3$ was
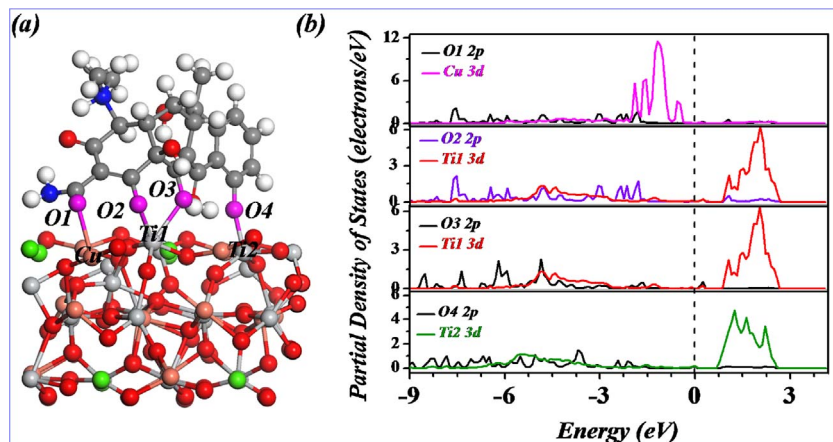

Fig. 9. (a) The calculated structure of TC adsorption at $CaCu_3Ti_4O_{12}$; (b) the corresponding partial density of states (PDOS) for interacting atoms at the adsorption site.
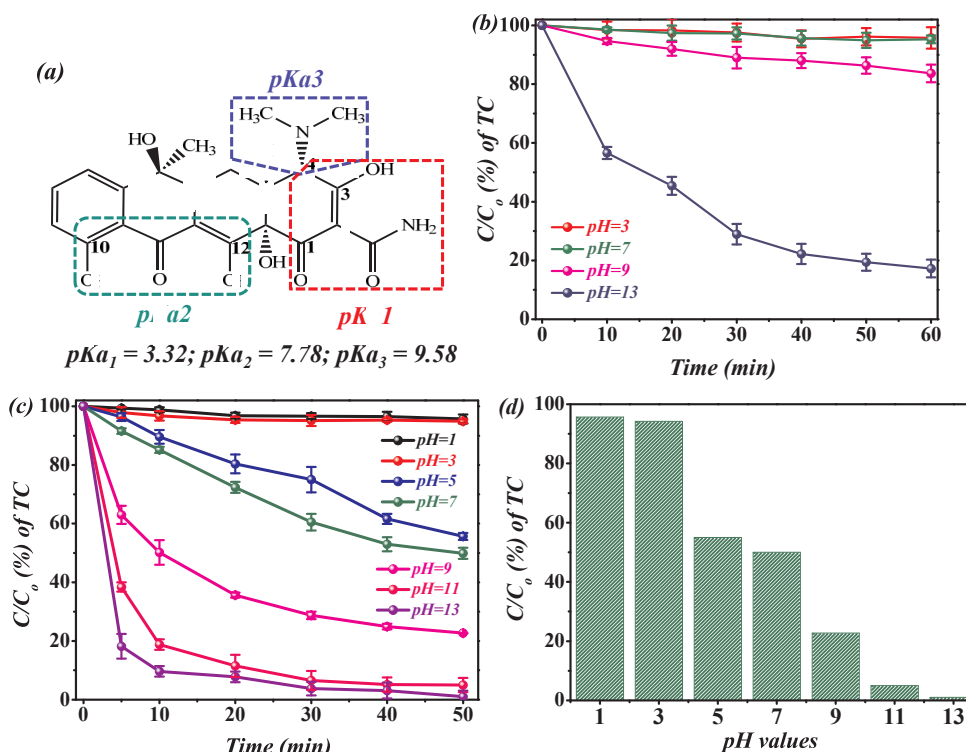
Fig. 10. (a) Molecular structure and p*K*a of TC; (b) Influence of initial pH on TC degradation in the absence of a photocatalyst; (c) Influence of initial pH on the photocatalytic degradation of TC in the presence of *Sample 5*; (d) Comparison of the photocatalytic degradation of TC in a wide range of pHs over the *Sample 5*.

presented as the e⁻ trapping agent at pH = 7.0 (Fig. 11b). This indicates that the photogenerated electrons, to some degree, are beneficial for degrading TC. On the contrary, the reaction is distinctly suppressed in the presence of PBQ and AO scavengers (the active radical trapping tests of TC over other samples are given in Figs. S5–S7, in the Supporting Information). These results show that $\cdot O_2^-$, photogenerated h^+ with synergetic role of e⁻ play major role and are largely responsible for decomposing TC degradation.

For further identifying involved reactive species, the electron spin resonance (ESR) measurements were carried out. Visible light irradiation for 5 min gave sextet strong characteristic peaks of the DMPO − $\cdot O_2^-$, clearly demonstrates the generation of $\cdot O_2^-$ in the studied system in the aqueous neutral solution (Fig. 11c). The characteristic signals of $\cdot OH$ were not detected, suggesting that the $\cdot OH$ almost not contributed to the oxidation of TC in neutral systems, which is consistence with the results of active radical trapping experiments (Fig. 11d). The spin label TEMPO was used to detect photoinduced electrons in studied samples with the corresponding stable triplet ESR characteristic signals with the strong intensity of 1: 1: 1 as depicted in Fig. 11e. For the further confirmation of photoinduced hole generation in the studied system, the spin lable CPH was added, and the triple characteristic ESR signals were captured (Fig. 11f), supporting that electrons on the VB were successfully excited to CB to generate more photoinduced holes in the solution. These results indicating the effective formations of electron–hole pairs, and further emphasizing the main roles of active species, which make huge contribution for TC decomposition.

On the basis of above trapping experiments and corresponding ESR analysis, it can be concluded that the superoxide radicals, holes and electrons (photoinduced and transferred) play dominant role for TC oxidation. On the other hand, it is obvious from the trapping test experiments that, TC solution favors the effective electron generation, which further accelerate production of more superoxide $\cdot O_2^-$ radicals as a result of $O_2 + e^- \rightarrow \cdot O_2^-$. These high amounts of $\cdot O_2^-$ accelerate TC decomposition. Additionally, it should be emphasized that the involved active species ($\cdot O_2-$, h^+ and e⁻) are affected by morphologies of samples, and no matter how changes the morphology of obtained samples, the photoinduced holes from valence band and superoxide

radicals play significant role for TC decomposition (Figs. S5–S7, in the Supporting Information). These results are in good agreements with previously reported one that the direct oxidation of TC by holes was more important in the titania catalysis [49]. Thus, both the degradation efficiency and involved radicals are strongly dependent on the properties of synthesized samples. Above experimental results and discussions give the clear evidence that the correlations between specific morphology and enhanced photocatalytic activity may be originated several factors, such as the abundance of defects, exposed facets, the charge distribution on the surface of photocatalyst, chemical environment as well as surface unsaturated atom sites. However, the photocatalytic degradation of TC over diverse morphological samples is a complex process since the probe molecular TC is pH sensitive and other factor should be taken into consideration, about which further investigations are currently under progress.

A detailed photodegradation study of trapping experiments shows that the various active species are responsible for TC photodegradation, which favors the production of active radicals resulting in enhanced degradation. With the assistance of aforementioned factors, TC mineralized eventually in the presence of $CaCu_3Ti_4O_{12}$ samples, which further testified by total organic carbon (TOC) measurements. The TOC removal (%) was calculated as follows [50]:

$$TOC\ removal(\%) = \frac{TOC_o - TOC_t}{TOC_o}$$

where TOC_o = initial TOC, in ppm; and TOC_t = varied TOC at given time t, in ppm. The approximately 89.58% TOC removal efficiency is achieved in the presence of *Sample 5* as depicted in Fig. 12. The higher decomposition efficiency (99.1%), FTIR and TOC results give evidence of complete mineralization of TC, and the organic carbon is converted to CO_2. The corresponding first-order rate constants of TC degradation over distinct morphological samples, surface property, TC adsorption as well as the TOC removal efficiency are summarized in Table 2.

4. Conclusions

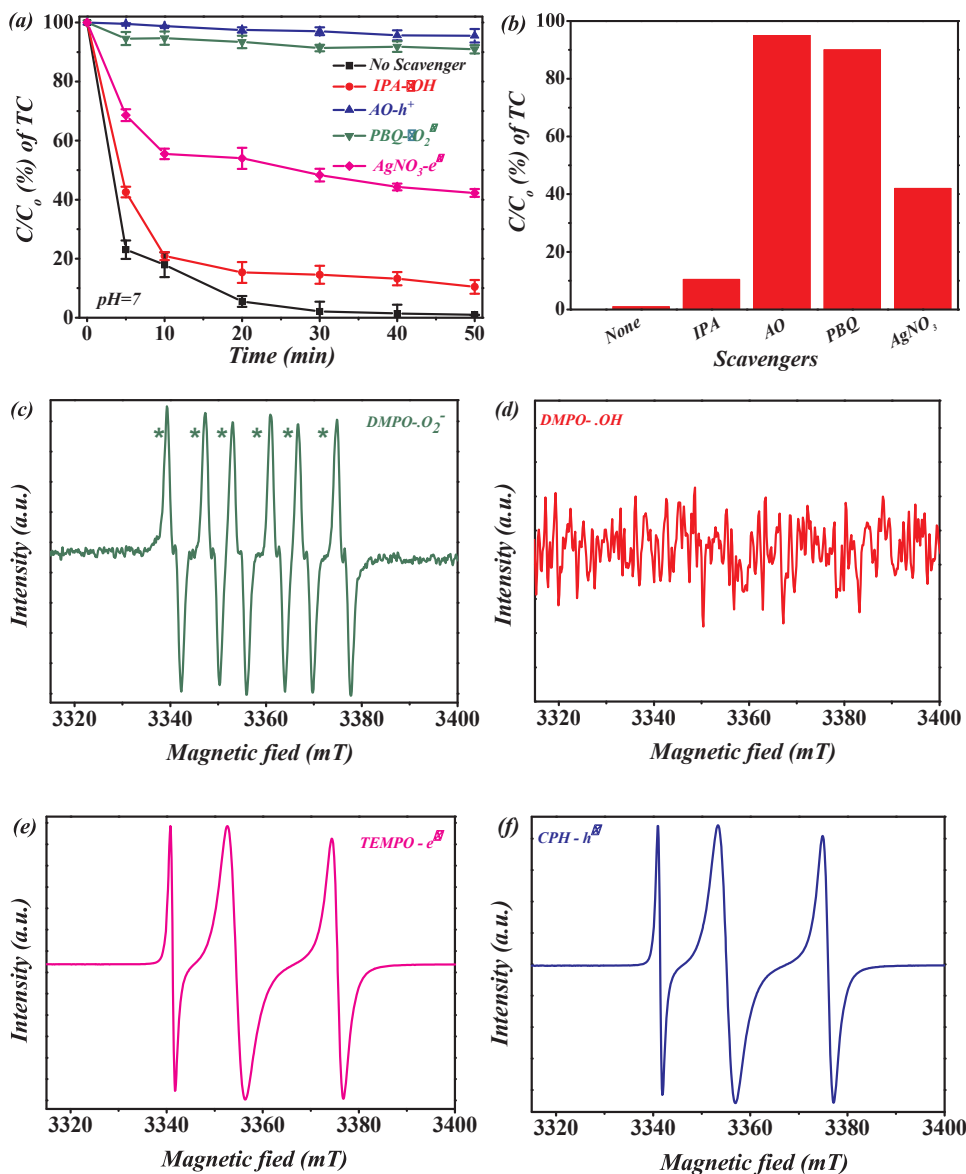In summary, various morphological Ti-based visible light active

Fig. 11. (a) Trapping experiments of active species for the degradation of TC over *Sample 5* at pH = 7.0; (b) Comparison results of trapping experiments of active species for the degradation of TC over *Sample 2*–*Sample 5* at pH = 7.0; (c–d) ESR detection of superoxide and hydroxyl radicals using a DMPO spin−trapping agent. The methanol/water solution of DMPO was preirradiated in the presence of *Sample 5*; (e–f) ESR detection of photoinduced electrons and holes with a TEMPO/CPH spin−trapping agent in the presence of *Sample 5*.

double perovskites $CaCu_3Ti_4O_{12}$ with oxygen deficiency were prepared via molten salt synthesis by adjusting the salt compositions, and applied as a promising photocatalyst for antibiotic degradation. Following four features were demonstrated in this work: (i) By altering the salt compositions with various cations (Li^+, Na^+, K^+) and anions (F^-, Cl^-, Br^-), the morphology tailoring was achieved at relatively low temperature and shorter reaction time (800 °C, 6 h), yet with the high

yields and well crystallinizations of the products; the formation mechanism of diverse morphology and effects of salt compositions were revealed. With simplicity and wide range of molten salt agent alteration, this synthetic method can be potentially applied as a general strategy for the controlled synthesis of earth-abundant element composed complex systems of visible light driven photocatalysts with efficient solar energy conversion for environmental remediation. (ii) As-
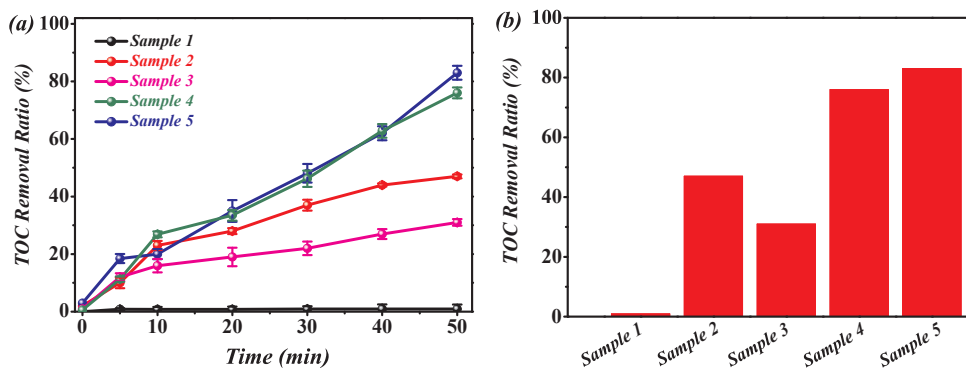

Fig. 12. TOC removal percentages of TC degradation in the presence of the *Sample 1*–*Sample 5* after 50 min visible-light irradiation.

Table 2

TC decomposition, surface property, kinetics, TC adsorption as well as TOC removal efficiency over distinct morphological $CaCu_3Ti_4O_{12}$ samples.

Sample no.	Morphology	Surface area ($m^2\,g^{-1}$)	TC degradation (%)	First-order rate constants k (min^{-1})	TC adsorption (%)	TOC removal (%)	Active species
Sample 1	Cube	6.2830	7.9128	5.6×10^{-4}	1.4790	0.94110	$\cdot O_2-,\, h^+$
Sample 2	Polyhedron	0.0940	87.361	5.1×10^{-2}	14.789	47.581	$\cdot O_2-,\, h^+$
Sample 3	Cube	4.0900	66.810	2.8×10^{-2}	15.557	31.249	$\cdot O_2-,\, h^+,\, e-$
Sample 4	Nanorods	17.670	97.152	8.4×10^{-2}	22.872	76.846	$\cdot O_2-,\, h^+,\, \cdot OH$
Sample 5	Octahedron	6.1070	99.143	1.1×10^{-1}	24.567	89.575	$\cdot O_2-,\, h^+,\, e-$

prepared samples exhibit defect related photocatalytic activity, working as an efficient photocatalysts with excellent decomposition property even after six runs degradation. Rationally tuning the compositions of molten salts, the structure property relationships and the correlations between oxygen vacancy−dependent photocatalytic properties were discussed. The abundant defects in the structure were found to be the main factor influencing photodecomposition efficiency. This finding provides green, economical synthesis and rational design of defect containing photocatalysts. (iii) Highlightly, as-obtained samples exhibit pH dependent activity in degradation of antibiotics and the efficiency is improved as the increasing of pH from 1.0 to 13.0, indicating potential application in the field of environmental science. (iv) By theoretical investigations of DFT calculation, this study disclosed the possible mechanism of antibiotic decomposition, and revealed that the enhanced interaction between tetracycline and photocatalysts is the main factor of improved efficiency. Existence of tetracycline at environment could be efficiently decomposed by photocatalyst under light irradiation. The present study could offer new motivations and present the possibilities of cost effective synthesis of other perovskite photocatalysts for the further investigations and will, in turn, provide some inspirations for pollutant degradation for the further practical implementations.

In the further investigation, the reaction conditions (calcination temperature and time, salt compositions, mole ratio of salts), introducing defects and doping with other transition metal elements will be investigated as promising candidates for visible light pollutant gradation and efficiency enhancement.

Acknowledgements

Appendix A. Supplementary data

Supplementary data associated with this article can be found, in the online version, at http://dx.doi.org/10.1016/j.apcatb.2017.09.026.

References

[1] W. Wang, M.O. Tade, Z.P. Shao, Chem. Soc. Rev. 44 (2015) 5371–5408.
[2] M.R. Hoffmann, S.T. Martin, W. Choi, D.W. Bahnemann, Chem. Rev. 95 (1995) 69–96.
[3] X. Lang, X.D. Chen, J.C. Zhao, Chem. Soc. Rev. 43 (2014) 473–486.
[4] C.C. Chen, W.H. Ma, J.C. Zhao, Chem. Soc. Rev. 39 (2010) 4206–4219.
[5] D.J. Martin, G.G. Liu, S.J.A. Moniz, Y.P. Bi, A.M. Beale, J.H. Ye, J.W. Tang, Chem. Soc. Rev. 44 (2015) 7808–7828.
[6] X.B. Chen, L. Liu, P.Y. Yu, S.S. Mao, Science 331 (2011) 746–749.
[7] A. Fujishima, K. Honda, Nature 238 (1972) 37–38.
[8] J.X. Bai, C.P. Sun, D. Liu, X.H. Luo, D. Li, J. Wang, N.X. Wang, X.J. Chang, R.L. Zong, Y.F. Zhu, Appl. Catal. B: Environ. 24 (2017) 11–20.
[9] F. Ronconi, Z. Syrgiannis, A. Bonasera, M. Prato, R. Argazzi, S. Caramori, V. Cristino, C.A. Bignozzi, J. Am. Chem. Soc. 137 (2015) 4630–4633.
[10] N. Zhang, X.Y. Li, H.C. Ye, S.M. Chen, H.X. Ju, D.B. Liu, Y. Lin, W. Ye, C.M. Wang, Q. Xu, J.F. Zhu, L. Song, J. Jiang, Y.J. Xiong, J. Am. Chem. Soc. 138 (2016) 8928–8935.
[11] K.F. Wu, Z.Y. Chen, H.J. Lv, H.M. Zhu, C.L. Hill, T.Q. Lian, J. Am. Chem. Soc. 136 (2014) 7708–7716.
[12] K. Maeda, K. Teramura, D.L. Lu, T. Takata, N. Saito, Y. Inoue, K. Domen, Nature 440 (2006) 295–295.
[13] A. Ishikawa, T. Takata, J.N. Kondo, M. Hara, H. Kobayashi, K. Domen, J. Am. Chem. Soc. 124 (2002) 13547–13553.
[14] Y.G. Zhou, Y.F. Zhang, M.S. Lin, J.L. Long, Z.Z. Zhang, H.X. Lin, J.C.-S. Wu, X.X. Wang, Nat. Commun. 6 (2015) 8340–8348.
[15] Z.Y. Zhang, Y.Z. Huang, K.C. Liu, L.J. Guo, Q. Yuan, B. Dong, Adv. Mater. 27 (2015) 5906–5914.
[16] Z.Y. Zhang, J.D. Huang, M.Y. Zhang, Q. Yuan, B. Dong, Appl. Catal. B: Environ. 163 (2015) 298–305.
[17] Q. Wang, T. Hisatomi, Q.X. Jia, H. Tokudome, M. Zhong, C.Z. Wang, Z.H. Pan, T. Takata, M. Nakabayashi, N. Shibata, Y.B. Li, I.D. Sharp, A. Kudo, T. Yamada, K. Domen, Nat. Mater. 15 (2016) 611–615.
[18] R. Hailili, G.H. Dong, Y.C. Ma, S. Jin, C.Y. Wang, T. Xu, Ind. Eng. Chem. Res. 56 (2017) 2908–2916.
[19] K. Iizuka, T. Wato, Y. Miseki, K. Saito, A. Kudo, J. Am. Chem. Soc. 133 (2011) 20863–20868.
[20] W.W. He, H.-K. Kim, W.G. Wamer, D. Melka, J.H. Callahan, J.J. Yin, J. Am. Chem. Soc. 136 (2014) 750–757.
[21] C.Y. Wang, D.W. Bahnemann, J.K. Dohrmann, Chem. Commun. 16 (2000) 1539–1540.
[22] C.Y. Wang, C. Bettcher, D.W. Bahnemann, J.K. Dohrmann, J. Mater. Chem. 13 (2003) 2322–2329.
[23] C.F. Ma, Y. Zhang, W.Q. Cui, Y.H. Liang, Y.F. Zhu, Appl. Catal. B: Environ. 212 (2017) 41–49.
[24] Y.X. Li, L. Zang, D.L. Jacobs, J. Zhao, X. Yue, C.Y. Wang, Nat. Commun. 8 (2017) 14466–14474.
[25] Y.F. Ji, Y. Luo, J. Am. Chem. Soc. 138 (2016) 15896–15902.
[26] H. Li, F. Qin, Z.P. Yang, X.M. Cui, J.F. Wang, L.Z. Zhang, J. Am. Chem. Soc. 139 (2017) 3513–3521.
[27] J.H. Clark, M.S. Dyer, R.G. Palgrave, C.P. Ireland, J.R. Darwent, M.J. Rosseinsky, J. Am. Chem. Soc. 133 (2011) 1016–1032.
[28] H.S. Kushwaha, N.A. Madhar, B. Ilahi, P. Thomas, A. Halder, R. Vaish, Sci. Rep. 6 (2016) 18557–18657.
[29] D.E. Woon Jr., T.H. Dunning, J. Chem. Phys. 98 (1993) 1358–1371.
[30] J.P. Perdew, K. Burke, M. Ernzerhof, Phys. Rev. Lett. 77 (1996) 3865–3868.
[31] X.G. Han, Q. Kuang, M.S. Jin, Z.X. Xie, L.S. Zheng, J. Am. Chem. Soc. 131 (2009) 3152–3153.
[32] S.W. Liu, J.G. Yu, M. Jaroniec, J. Am. Chem. Soc. 132 (2010) 11914–11916.
[33] H.G. Yang, C.H. Sun, S.Z. Qiao, J. Zou, G. Liu, S.C. Smith, H.M. Cheng, G.Q. Lu, Nature 453 (2008) 638–641.
[34] R. Li, F. Zhang, D. Wang, J. Yang, M. Li, J. Zhu, X. Zhou, H. Han, C. Li, Nat. Commun. 4 (2013) 1432–1439.
[35] L. Wang, L. Zang, J.C. Zhao, C.Y. Wang, Chem. Commun. 48 (2012) 11736–11738.
[36] Y.X. Li, L. Zang, Y. Li, Y. Liu, C.Y. Liu, Y. Zhang, H.Q. He, C.Y. Wang, Chem. Mater. 25 (2013) 2045–2050.
[37] Y.X. Li, B.R. Bunes, L. Zang, J. Zhao, Y. Li, Y.Q. Zhu, C.Y. Wang, ACS Nano 10 (2016) 2386–2391.
[38] Y.X. Li, G. Chen, Q. Wang, X. Wang, A.K. Zhou, Z.Y. Shen, Adv. Funct. Mater. 20 (2010) 3390–3398.
[39] S.Q. Deng, G. Xu, H.W. Bai, L.L. Li, S. Jiang, G. Shen, G.R. Han, Inorg. Chem. 53 (2014) 10937–10943.
[40] P. Kubelka, F. Munk, Z. Tech. Phys. 12 (1930) 593–601.
[41] X.J. Luo, Y.S. Liu, C.P. Yang, S.S. Chen, S.L. Tang, K. Bärner, J. Eur. Ceram. Soc. 35 (2015) 2073–2081.
[42] G.M. Zeng, M. Chen, Z.T. Zeng, Science 340 (2013) 1403.
[43] J.M. Buriak, P.V. Kamat, K.S. Schanze, ACS Appl. Mater. Interfaces 6 (2014) 11815–11816.
[44] Z.Y. Zhang, J.H. Huang, Y.R. Fang, M.Y. Zhang, K.C. Liu, B. Dong, Adv. Mater. 29 (2017) 1606688.
[45] Z.Y. Zhang, K.C. Liu, Y.N. Bao, B. Dong, Appl. Catal. B: Environ. 203 (2017) 599–606.
[46] Y. Xu, M.A.A. Schoonen, Am. Miner. 85 (2000) 543–556.
[47] Q. Liu, Y. Zhou, J.H. Kou, X.Y. Chen, Z.P. Tian, J. Gao, S.C. Yan, Z.G. Zou, J. Am. Chem. Soc. 132 (2010) 14385–14387.
[48] H. Wang, H. Yao, P. Sun, D. Li, C.H. Huang, Environ. Sci. Technol. 50 (2016) 145–153.
[49] K. Dai, T.Y. Peng, H. Chen, R.X. Zhang, Y.X. Zhang, Environ. Sci. Technol. 42 (2008) 1505–1510.
[50] X.K. Li, N. Kikugawa, J.H. Ye, Adv. Mater. 20 (2008) 3816–3819.